Manuscript Number:	
Full Title:	Structure, magnetocaloric effect and critical behaviour in Ni50Mn30(Sn,In)20 Heusler alloys
Article Type:	Original Research
Keywords:	NiMn-based alloys; Magnetic transition; Critical behavior; Magnetocaloric effect; Landau theory.
Corresponding Author:	Safia Alleg, PhD Badji Mokhtar Annaba University Annaba, ALGERIA
Corresponding Author Secondary Information:	
Corresponding Author's Institution:	Badji Mokhtar Annaba University
Corresponding Author's Secondary Institution:	
First Author:	Karima Dadda, PhD
First Author Secondary Information:	
Order of Authors:	Karima Dadda, PhD
	Safia Alleg, PhD
	Joan J. Suñol, PhD
	Lotfi Bessais, PhD
	El Kebir Hlil, PhD
Order of Authors Secondary Information:	
Funding Information:	

Structure, magnetocaloric effect and critical behaviour
in Ni₅₀Mn₃₀(Sn,In)₂₀ Heusler alloys

K. Dadda[1], S. Alleg[1,*], J.J. Suñol[2], L. Bessais[3], E.K. Hlil[4]

[1]Laboratoire de Magnétisme et Spectroscopie des Solides (LM2S), Département de Physique, Université Badji Mokhtar Annaba, B.P. 12, Annaba 23000, Algérie.
[2]Dept. Fisica, Universitat de Girona, Campus Montillivi, Girona 17071 Spain.
[3]Université Paris–Est, ICMPE (UMR 7182) CNRS-UPEC, Thiais, F-94320, France.
[4]Institut Néel, CNRS, Université Grenoble Alpes, 25 Rue des Martyrs BP 166, F-38042 Grenoble Cedex 9, France.
Corresponding author e-mails: safia.alleg@univ-annaba.dz; safia_alleg@yahoo.fr
Tel: +213 671 228 079

Abstract

A detailed investigation of structure, critical behaviour and magnetocaloric properties of Ni₅₀Mn₃₀Sn₂₀ (Sn20) and Ni₅₀Mn₃₀In₂₀ (In20) alloys has been investigated by means of X-rays diffraction and magnetic measurements. Ni₅₀Mn₃₀Sn₂₀ alloy shows a cubic austenite $L2_1$ structure, and undergoes a second order magnetic transition at a Curie temperature of $T_{c,1}^A(Sn20) = 333\,K$. However, the Ni₅₀Mn₃₀In₂₀ alloy exhibits a mixture of cubic $L2_1$ and $B2$ austenite structures having Curie temperatures of $T_{c,2}^A(In20) = 285\,K$ and $T_c^*(In20) = 330\,K$, respectively. The modified Arrott plots, Kouvel-Fisher curves and critical isotherm analysis have been used to estimate the critical exponents (β, γ, and δ) around the Curie temperature. For Sn₂₀ alloy, the reliable exponents are consistent with the mean field model, revealing long-range ferromagnetic interactions. Nevertheless, the critical exponents of In₂₀ alloy around 330 K cannot be arranged into any of the universality classes of well-known classical standard models. The maximum entropy change under 5 T of Sn20 ($\Delta S_M^{max} = 2.43\,\frac{J}{kg}.K$) is slightly higher than that of In20 ($\Delta S_M^{max} = 2.05\,\frac{J}{kg}.K$). The experimental results of entropy changes are in good agreement with those calculated using Landau theory.

Keywords: NiMn-based alloys; Magnetic transition; Critical behavior; Magnetocaloric effect; Landau theory.

1. Introduction

Heusler alloys have attracted considerable attention due to their several technological applications such as sensors, spintronic devices and magnetic refrigeration [1-3]. Several experimental [4, 5] and theoretical [6, 7] studies have been carried out to investigate the properties of Heusler alloys. Off-stoichiometric NiMn-based ferromagnetic alloys exhibit an exchange bias phenomena (EB) [8], magnetoresistance [9, 10], magnetocaloric effect (MCE) [11, 12], magnetic super-elasticity [13] and piezoresistance [14]. It has been reported that $Ni_{50}Mn_{50-x}Sn_x$ series crystallize in a cubic austenite $L2_1$ structure, space group $Fm\bar{3}m$, for $x \geq 15$, and a martensite structure for $x < 15$ [15, 16]. An extended annealing of $Ni_{50}Mn_{39}Sn_{11}$ and $Ni_{50}Mn_{37}Sn_{13}$ alloys at $773\,K$, involves a phase decomposition of the eutectoid-type structure into $Ni_{54}Mn_{45}Sn_1$ and $Ni_{50}Mn_{30}Sn_{20}$. Wherein, the Curie temperature was about $350\,K$ [17]. The standard enthalpy of formation, $\Delta_f H°$, of $Ni_{50.6}Mn_{29.6}Sn_{19.8}$ alloy was $-21.0\,kJ/mol\ of\ atom$ [18]. A linear shift of the reverse and forward martensitic transition temperatures in $Ni_{46.4}Mn_{32.8}Sn_{20.8}$ alloy occurs by high magnetic field application up to $14\,T$ [19]. Moreover, a spin glass behaviour was found in $Ni_{50}Mn_{30}Sn_{20}$ alloy [20]. For Ni-Mn-In alloys, the structural transition was observed in Mn-rich composition where both the austenite and martensite phases exhibit a ferromagnetic order [21, 22]. Krenke *et al.* reported that $Ni_{50}Mn_{50-x}In_x$ alloys with $0.16 \geq x \geq 0.05$ show a first order structural transformation, and the Curie temperature decreases from 310 K for $x = 20$ to 290 K for $x = 25$ [23]. Furthermore, the martensitic transition temperature MT is influenced by change in elemental composition through the change of valence electron concentration per atom (*e/a*).

Depending on the nature of the magnetic transition, the magnetocaloric effect can be categorised. For the second order magnetic transition, the resulted negative entropy change around the Curie temperature of the austenite structure, T_c^A, produces a direct MCE. However, an inverse magnetocaloric effect, $IMCE$, is engendered with a positive value of the entropy change around the martensitic transformation, MT. The existence of a universal behavior in materials can be investigated through the critical exponents (β, γ and δ) associated with the phase transitions. By using several models [24] such as the mean field model associated with long-range mean field theory where $\beta = 0.5$ and $\gamma = 1$, short-range interactions as specified by the Heisenberg model with $\beta = 0.365$ and $\gamma = 1.336$, 3D-Ising model with $\beta = 0.325$ and $\gamma = 1.241$, and tricritical mean field model with $\beta = 0.25$ and $\gamma = 1$, the critical exponents β, γ and δ can be estimated from the isothermal magnetization curves, $M(H)$. The exponent β, which is linked to the evolution of the spontaneous magnetization with respect to

the temperature ($M_s \propto (T - T_c)^{\beta}$), describes the growth of the ordered moment below T_c; γ is related to the temperature dependence of the initial magnetic susceptibility ($\chi_0^{-1} \propto (T - T_c)^{\gamma}$). It defines the divergence of χ_0 at T_c, and δ is associated to the critical isothermal magnetization. It describes the curvature of the isothermal magnetization curves $M(H)$ at T_c. The mechanisms of magnetic phase transitions are to some extent vague due to the influence of many parameters such as the preparation method, the alloy composition, the thermal history, etc. Consequently, the aim of the present work is to investigate the magnetocaloric effect and the critical behaviour near the Curie temperature in the melt spun $Ni_{50}Mn_{30}(Sn, In)_{20}$ ribbons.

2. Experimental details

Polycrystalline alloys with nominal compositions of $Ni_{50}Mn_{30}Sn_{20}$ and $Ni_{50}Mn_{30}In_{20}$, henceforth called Sn20 and In2, respectively, have been prepared by arc melting high purity elements Ni, Mn, Sn and In (99.9 %) under an argon atmosphere. The ingots were re-melted five times to ensure homogeneity. Sn20 and In20 alloys ribbons have been elaborated by melt spinning onto a surface of copper wheel rotating at a linear speed of 40 m/s under argon atmosphere. The crystal structure was checked by X−ray diffraction (XRD) on a Brüker D8 Advance diffractometer using Cu-Kα radiation (λ_{Cu} = 0.154056 nm) in a $\theta - 2\theta$ Bragg Brentano geometry. The XRD patterns were computer refined using the MAUD program which is based on the Rietveld method [25]. Magnetization measurements were carried out in a superconducting quantum interference device (SQUID) magnetometer and a BS2 magnetometer developed at the Néel Institute under an applied magnetic field of 0.05 T. The critical exponents and the magnetic entropy changes around the Curie temperature have been determined from the isothermal magnetization measurements as a function of the applied magnetic field.

3. Results and discussion

Figure 1 and Figure 2 show the Rietveld refinement of the XRD patterns of Sn20 and In20 alloys, respectively. The XRD patterns exhibit thin and intense peaks characteristic of a fully crystalline microstructure due to the fast crystallization and growth kinetics of the samples during the melt spinning process. One observes also that the peak intensities of Sn20 are slightly high than those of In20. The high order of $L2_1$ austenite in both alloys is confirmed by the superlattice (111), (311) and (311) reflections. In addition, Sn20 is a textured alloy as shown by (311) reflection intensity. Such preferential orientation might be

due to fact that during the rapid solidification, the heat removal induces directional growth of the crystalline phase. The importance of (111) and (311) peaks intensity compared to those obtained in the $Ni_{50}Mn_{30}Sn_{20}$ Heusler alloy prepared by arc melting followed by annealing at 1000°C for 24 h [20], confirms the effect of the preparation method on the structural properties. Usually the non-stoichiometry of the alloy with a low content of Z element gives rise to weak minor peaks of the superstructure in Heusler alloys. While the Sn20 alloy show a single austenite $L2_1$ structure (lattice parameter a=0.5994(3) nm, space group $Fm\bar{3}m$), the In20 alloy exhibit a mixture of an ordered $L2_1$ phase, (volume fraction ~85 %, and lattice parameter $a = 0.6088(3)\,nm$), and a partially ordered $B2$ phase (space group $Pm\bar{3}m$, volume fraction ~15 % and lattice parameter $a = 0.3011(2)\,nm$). The formation of $B2$ structure can be linked to the degree of atomic order.

The temperature dependence of the magnetization, $M(T)$, recorded at 0.05 T for both Sn20 and In20 alloys, is displayed in Fig. 3. The Curie temperature was inferred from the minimum in dM/dT *versus* temperature curve as shown by the inset in Fig. 3. For the Sn20 alloy, the ferromagnetic to paramagnetic transition $T_c^A(Sn20)$ occurs at $333\,K$, whereas the In20 alloy displays two magnetic transition temperatures at $285\,K$ and $330\,K$ that can be attributed to $L2_1$ and $B2$ structures, respectively. This result agrees well with the XRD one and confirms thus the biphasic character of In20 alloy. The magnetic transitions of both phases are different from those reported in the literature [26-28]. Those discrepancies might be ascribed to the composition change and/or the preparation conditions. For example, the obtained lower Curie temperature (Tc~ 222 K) for the austenite phase by R.C. Bhatt et al. [20], has been attributed to deficiency of Sn atoms in the system.

The isothermal magnetization curves of In20 and Sn20 alloys, $M(H)$, around the Curie temperature are presented in Fig. 4 as a function of the applied magnetic field up to 6 T. For both alloys, the magnetization does not saturate even at 5 T. In the magnetic system, the *MCE* is related to the magnetic entropy change, ΔS_M which might be induced by an applied magnetic field that leads to the change in the magnetic order. The magnetic entropy change ΔS_M can be deduced from the isothermal magnetization, $M(H)$, curves *via* the following Maxwell relation:

$$\Delta S_M(T, \Delta H) = S_M(\text{T}, H_2) - S_M(T, H_1) = \int_{H_1}^{H_2} \left(\frac{\partial M}{\partial T}\right)_T dH \qquad (1)$$

Where H_1 and H_2 are the applied magnetic fields with $H_1 < H_2$, and $\Delta H = H_2 - H_1$. ΔS_M can be calculated by integrating the $M(H)$ curves at small discrete magnetic field and temperature intervals, and can be approximated by the succeeding equation:

4

$$\Delta S_M(T,M) = \sum_i \frac{M_{i+1}(T_{i+1},H_{i+1}) - M_i(T_i,H_i)}{T_{i+1}-T_i} \Delta H \qquad (2)$$

Where M_i and M_{i+1} are the experimental data of the magnetization at T_i and T_{i+1}, respectively, under the magnetic field H_i. The variation of $-\Delta S_M$ as a function of the temperature is shown in Fig. 5. The maximum magnetic entropy change, $-\Delta S_M^{max}$, increases with increasing the applied magnetic field and reaches 2.43 J/kg.K for Sn20, and 2.05 J/kg.K for In20 (see the inset in Fig. 5). One notes that $-\Delta S_M^{max}$ value of Sn20 alloy is $\sim 16\%$ higher than that obtained in $Ni_{50}Mn_{35}Sn_{15}$ alloy prepared in the same conditions [29].

The relative cooling power, RCP, associated with the magnetic entropy change is an important feature to evaluate the magnetocaloric efficacy of materials. The relative cooling power is given by the following equation:

$$RCP = -\int_{T_1}^{T_2} \Delta S_M(T)dT \qquad (3)$$

Where T_1 and T_2 temperatures are defined by the full width at half maximum of $\Delta S_M(T)$ peak. For Sn20 and In20 ribbons, the calculated RCP values are of about 172.88 J/kg and 240 J/kg, respectively, for an applied magnetic field of 5 T. The RCP value of Sn20 is much higher than that obtained for the same composition by Bhatt et al. ($RCP = 54.6\,J/kg$) under a magnetic field of 3 T [20].

Amaral *et al.* proposed a theoretical model based on the contribution of the magneto-elastic interactions of electrons [30] and on Landau theory in the critical region [31]. The free energy (G) is developed as a function of the magnetization (M):

$$G(M,T) = G_0 + \frac{a(T)}{2}M^2 + \frac{b(T)}{4}M^4 + \frac{c(T)}{6}M^6 + \cdots\cdots - HM \qquad (4)$$

For the equilibrium condition, $\partial G/\partial M = 0$, the total magnetization in the critical region is given by the following relationship:

$$H = a(T)M + b(T)M^3 + c(T)M^5 \qquad (5)$$

The Landau's coefficient $a(T)$, $b(T)$ and $c(T)$ are determined from the polynomial fit of the experimental $M(H)$ data according to the Eq.5. The variation of $a(T)$ shows a minimum around T_c^A, and $b(T_c^A) = 0$ proves the second order character of the magnetic transition. The derivative of the free energy with respect to the temperature gives a theoretical model of the magnetic entropy change:

$$-\Delta S_M(T,H) = \left(\frac{dG}{dT}\right)_H = \frac{a'(T)}{2}M^2 + \frac{b'(T)}{4}M^4 + \frac{c'(T)}{6}M^6 \qquad (6)$$

where $a'(T)$, $b'(T)$ and $c'(T)$ are the derivative of Landau's coefficients with respect to the temperature. The calculated $-\Delta S_M$ curves are in a good agreement with the experimental results (Fig. 7). Thus, the calculated Landau's coefficients are accurate.

5

In order to understand the interaction type of the magnetic moments and the universality class of Sn20 and In20 ribbons, the critical exponents have been analysed through different techniques such as the modified Arrott plots (MAP) [32], Kouvel-Fisher plots ($K - F$) [33, 34] and critical isotherm (CI). Hence, the critical exponents β, γ and δ can be determined using Equations 7-9:

$$M_S(T) = M_0(-\varepsilon)^\beta; \ \varepsilon < 0, \ T < T_c \tag{7}$$

$$\chi_0^{-1}(T) = \left(\frac{h_0}{M_0}\right)\varepsilon^\gamma; \ \varepsilon > 0, \ T > T_c \tag{8}$$

$$M = DH^{1/\delta}; \ \varepsilon = 0, T = T_c \tag{9}$$

where $M_S(T)$ and $\chi_0^{-1}(T)$ are the spontaneous magnetization and the inverse initial magnetic susceptibility, respectively; $\varepsilon = (T - T_c)/T_c$ is the reduced temperature; M_0, h_0, and D are the critical amplitudes.

The magnetic interactions that characterize a magnetic system can be described by four distinct conventional models: the mean field model, 3D-Heisenberg model, 3D-Ising model, and tricritical mean field model [24]. The modified Arrott plots around the Curie temperature of $L2_1$ structure are shown in Figures 8 and 9. The calculated relative slopes, RS, identified as the slope at each temperature T to the slope at the critical temperature ratio, are plotted using the linear fit from the high field region of each curve (Fig. 10). In the ordered $L2_1$ structures, the mean field model is the best model that describes both In20 and Sn20 ribbons since RS are much closer to 1. By fitting the spontaneous magnetization $M_s(T, 0)$ and the inverse of the initial susceptibility $\chi_0^{-1}(T, 0)$ curves using equations 7 and 8, respectively, the new values of β, γ and T_c^A (table 1) can be determined (Fig. 11). One notes that the β and γ values are close to the mean field model with a long range order of magnetic interactions, and the Curie temperatures are close to those obtained from the $M(T)$ curves.

The Kouvel-Fisher plots of $M_S(T)(dM_S(T)/dT)^{-1}$ and $\chi_0^{-1}(T)(d\chi_0^{-1}(T)/dT)^{-1}$ against the temperature (Fig. 12) show straight lines with slopes $1/\beta$ and $1/\gamma$, respectively. Moreover, the β and γ exponent values are interconnected to the third exponent δ *via* the Widom scaling relation ($\delta = 1 + (\gamma/\beta)$) [35]. The calculated δ values (table 1) are comparable to those estimated from the CI curves (Fig. 13). The validity of the critical exponents and the Curie temperature values are confirmed by the scaling hypothesis [36] through the following equation:

$$M(H, \varepsilon) = \varepsilon^\beta f_\pm\left(H/\varepsilon^{\beta+\gamma}\right) \tag{10}$$

6

The regular analytic functions f_+ and f_- are undertaken for $T > T_c^A$ and $T < T_c^A$, respectively. The $M|\varepsilon|^{-\beta}$ as a function of $H|\varepsilon|^{-(\beta+\gamma)}$ are plotted in the vicinity of the Curie temperature (Fig. 14). The presence of two distinct branches below and above T_c^A confirms the fact that the predicted critical exponents and Curie temperatures are reasonably accurate.

The modified Arrott plots of the disordered cubic $B2$ structure around $T_c^*(In20) = 330\ K$ show curved lines rather than straight-lines (Fig. 15), and the linear fit at high field region has negative intercept. Accordingly, those models are unable to describe the system. The exponents values were obtained from the optimum fitting of $M_s(T, 0)$ and $\chi_0^{-1}(T, 0)$ curves using Eq.(7) and Eq.(8), respectively, which were determined from the high field region of $M^{1/\beta}$ against $(\mu_0 H/M)^{1/\gamma}$ plot. This process was repeated several times until the convergence. The nonlinear fit to the $M_s(T, 0)$ and $\chi_0^{-1}(T, 0)$ plots gives $\beta = 0.434 \pm 0.037$, $\gamma = 0.737 \pm 0.490$ and $T_c^* = (331.328 \pm 0.919)\ K$ values (Fig. 16). As shown in Fig. 17, the modified Arrott plot presents almost parallel isotherms near T_c^* by using the unconventional exponents. The Kouvel-Fisher plots are presented in Fig. 18, and the convergence was reached with nearby values to those obtained from the modified Arrott plots with $\beta = 0.466 \pm 0.050$, $\gamma = 0.702 \pm 0.043$ and $T_c^* = (331.420 \pm 1.142)\ K$. The validity of those unconventional critical exponents and T_c^* values were confirmed by the scaling hypothesis as shown in Fig. 19. The third exponent δ was determined experimentally from the critical curve $M = f(H, T_c^*)$ (Fig. 20), and analytically by the Widom scaling relation. The experimental and calculated δ values were $\delta = 2.645 \pm 0.003$ and $\delta_{cal} = 2.698 \pm 0.453$, respectively. The critical exponents of Sn20 and In20 alloys as well as those of the different models are reported in Table 1. One observes that β have smaller values indicating a faster growth of the ordered moment. The initial susceptibility has a softer divergence at $T_c^A(Sn20)$ and $T_c^A(In20)$, and sharper divergence at $T_c^*(In20)$. The δ values reflect the faster saturation of $M(H)$ curves at T_c^A, the less curvature and slower saturation at T_c^*.

4. Conclusion

Structure, magnetocaloric effect and critical behaviour of the $Ni_{50}Mn_{30}(Sn,In)_{20}$ alloys were studied. Sn20 ribbons exhibit a single cubic $L2_1$ structure and undergo a second order magnetic transition at 333 K. The presence of $L2_1$ and $B2$ structures in the In20 ribbons is confirmed by the existence of two Curie temperatures ($T_c^A = 285\ K$ and $T_c^* = 330\ K$). Magnetic entropy change, RCP and critical exponents' values of Sn20 are higher than those of In20. The mean field model, with long-range ferromagnetic interactions, was the best model

that describes the magnetic interactions around T_c^A. However, the critical exponents values around T_c^* are different from the well-known universality class.

Acknowledgements

8

References

1.   T. Tadaki, K.O., K. Shimizu,, *Shape Memory Alloys.* Annual Review of Materials Science, 1988. **18**: p. 25-45.

2.   K. Otsuka, X.R., *Recent developments in the research of shape memory alloys.* Intermetallics, 1999. **7**: p. 511-528.

3.   K. Sattler, *Handbook of nanophysics: Functional nanomaterials.* 2010.

4.   R. Topkaya, R.Y., S. Kazan, N. Akdoğan, M. Obaida, H. İnam, K. Westerholt, , *Annealing Effect on Structural and Magnetic Properties of Cu2MnAl Heusler Alloy Films.* Journal of Superconductivity and Novel Magnetism, 2012. **25**: p. 2605-2609.

5.   L. Y. Wang, X.T.W., L. Chen, Y. Zhang, Q. L. Xia, G. D. Liu, , *The Synthesis and Martensitic Transformation of the Co2TiSb1–xSnx(x = 0, 0.25, 0.5) Heusler Alloys.* Journal of Superconductivity and Novel Magnetism, 2016. **29**: p. 995-1000.

6.   V. K.Jain, N.L., R. Jain, A. R. Chandra, , *Electronic Structure, Elastic, Magnetic, and Optical Properties of Fe2MnZ (Z = Si, Ge, and Sn) Full Heusler Alloys: First-Principle Calculations.* Journal of Superconductivity and Novel Magnetism, 2019. **32**: p. 739-749.

7.   Dj. Mokhtari, H.B., Dj. Guendouz, Z. Charifi, B. Hamad, , *Theoretical Investigation of Structural, Electronic, Magnetic, and Mechanical Properties of Quaternary Heusler Alloys CoVTiX (X = As, Si).* Journal of Superconductivity and Novel Magnetism, 2018. **31**: p. 3625-3636.

8.   A. Çakır, M.A., M. Farle,, *Exchange bias caused by field-induced spin reconfiguration in Ni-Mn-Sn.* Physical Review B, 2016. **93**: p. 094411.

9.   A. Ghosh, K.M., *Large magnetic entropy change and magnetoresistance associated with a martensitic transition of Mn-rich Mn50.5–xNi41Sn8.5+x alloys.* Journal of Physics D: Applied Physics, 2013. **46**: p. 435001.

10.   L. Huang, D.Y.C., L. Ma, Z. H. Nie, M. G. Wang, Z. L. Wang, H. L. Suo, Y. Ren, Y. D. Wang, *Large magnetic entropy change and magnetoresistance in a Ni41Co9Mn40Sn10 magnetic shape memory alloy.* Journal of Alloys and Compounds, 2015. **647**: p. 1081-1085.

11.   T. Krenke, E.D., M. Acet, E. F. Wassermann, X. Moya, L. Mañosa, A. Planes., *Inverse magnetocaloric effect in ferromagnetic Ni-Mn-Sn alloys.* Nature Materials, 2005. **4**: p. 450.

12.   B. Hernando, J.L.S.L., J. D. Santos, V. M. Prida,   D. Baldomir, D. Serantes, R. Varga, J. González, *Magnetocaloric effect in melt spun Ni50.3Mn35.5Sn14.4 ribbons.* Applied Physics Letters, 2008. **92**: p. 132507.

13.   T. Krenke, E.D., M. Acet, E. F. Wassermann, X. Moya, L. Mañosa, A. Planes, E. Suard, B. Ouladdiaf., *Magnetic superelasticity and inverse magnetocaloric effect in Ni-Mn-In.* Physical Review B, 2007. **75**: p. 104414.

14.   L. Porcar, D.B., P. Courtois, *Large piezoresistance and magnetoresistance effects on Ni45Co5Mn37.5In12.5 single crystal.* Applied Physics Letters, 2012. **100**: p. 152405.

15.   T. Krenke, M.A., E. F. Wassermann, X. Moya, L. Mañosa, A. Planes, *Martensitic transitions and the nature of ferromagnetism in the austenitic and martensitic states of Ni-Mn-Sn alloys.* Physical Review B, 2005. **72**: p. 014412.

16.   A. Çakır, L.R., F. Albertini, M. Acet, M. Farle, *Intermartensitic transitions and phase stability in Ni50Mn50-xSnx*

Heusler alloys. Acta Materialia, 2015. **99**: p. 140–149.

17.   W. M. Yuhasz, D.S., Q. Xing, R. W. McCallum, T. Lograsso, , *Metastability of ferromagnetic Ni–Mn–Sn Heusler alloys.* Journal of Alloys and Compounds 2010. **492**: p. 681-684.

18.   M. Yin, P.N., W. Chen, S. Chen, , *Standard enthalpies of formation of selected Ni2YZ Heusler compounds.* Journal of Alloys and Compounds, 2016. **660**: p. 258-265.

19.   P. Lazpita, V.C., J. M. Barandiarán, I. Orue, J. Gutiérrez, J. Feuchtwanger, J. A. Rodriguez-Velamazán,, *Influence of Magnetic Field on Magnetostructural Transition in Ni 46.4 Mn 32.8 Sn 20.8 Heusler Alloy.* 2009. **635**: p. 89-95.

20. R. C. Bhatt, R.S.M., H. Kishan, V. P. S. Awana, S. K. Agarwal, *Structural, Magnetic and Magneto-caloric studies of Ni50Mn30Sn20Shape Memory Alloy.* Journal of Superconductivity and Novel Material, 2016. **29**: p. 3201-3206.

21. J. L. Sánchez Llamazares, T.S., J. D. Santos, M. J. Pérez, M. L. Sanchez, B. Hernando, L. Escoda, J. J. Suñol, R. Varga *Martensitic phase transformation in rapidly solidified Mn50Ni40In10 alloy ribbons.* Applied Physics Letters, 2008. **92**: p. 012513.

22. Y. Sutou, Y.I., N. Koeda, T. Omori, R. Kainuma, K. Ishida, K. Oikawa., *Magnetic and martensitic transformations of NiMnX„(X=In,Sn,Sb) ferromagnetic shape memory alloys.* Applied Physics Letters, 2004. **85**: p. 4358-4360.

23. T. Krenke, M.A., E. F. Wassermann, X. Moya, L. Mañosa, A. Planes, *Ferromagnetism in the austenitic and martensitic states of Ni-Mn-In alloys.* Physical Review B, 2006. **73**: p. 174413.

24. *<14722.pdf>.*

25. L. Lutterotti, S.M., H. R. Wenk, , *MAUD: a friendly Java program for material analysis using diffraction.* Newsletter of the CPD, 1999. **21**: p. 14-15.

26. A. Çakır, M.A., U. Wiedwald, T. Krenke, M. Farle, , *Shell-ferromagnetic precipitation in martensitic off-stoichiometric Ni-Mn-In Heusler alloys produced by temper-annealing under magnetic field.* Acta Materialia, 2017. **127**: p. 117-123.

27. J. L. Sánchez Llamazares, H.F.-Z., C. Sánchez-Valdes, C. A. Ross, C. García, , *Refrigerant capacity of austenite in as-quenched and annealed Ni51.1Mn31.2In17.7 melt spun ribbons.* Journal of Applied Physics, 2012. **111**: p. 07A932.

28. T. Sanchez, J.L.S.L., B. Hernando, J. D. Santos, Ml. Sanchez, M. J. Perez, J. J. Suñol, R. Turtelli, R. Grössinger, , *Annealing Effect on Martensitic Transformation and Magneto-Structural Properties of Ni-Mn-In Melt Spun Ribbons.* Materials Science Forum, 2009. **635**: p. 81-87.

29. K. Dadda, S.A., S. Souilah, J. J. Suñol, E. Dhahri, L. Bessais, E. K. Hlil, , *Critical behavior, magnetic and magnetocaloric properties of melt-spun Ni50Mn35Sn15 ribbons.* Journal of Alloys and Compounds, 2018. **735**: p. 1662-1672.

30. V. S. Amaral, J.S.A., *Magnetoelastic coupling influence on the magnetocaloric effect in ferromagnetic materials.* Journal of Magnetism and Magnetic Materials, 2004. **272-276**: p. 2104-2105.

31. L.D. Landau, E.M.L., *Statistical Physics part 2.* Course of theoritical physics, ed. P.I. Library. 1958, Oxford, New York: M. C. Robert Maxwell.

32. A. Arrott, *Criterion for Ferromagnetism from Observations of Magnetic Isotherms.* Physical Review, 1957. **108**(6): p. 1394-1396.

33. M. E. Fisher, S.k.M., B. G. Nickel, *Critical Exponents for Long-Range Interactions.* Physical Review Letters, 1972. **29**: p. 917-920.

34. J. S. Kouvel, M.E.F., *Detailed Magnetic Behavior of Nickel Near its Curie Point.* Physical Review 1964. **136**: p. A 1626.

35. B. Widom, *Surface Tension and Molecular Correlations near the Critical Point.* Journal of Chemical Physics, 1965. **43**: p. 3892-3897.

36. H. E. Stanley, *Introduction to Phase Transitions and Critical Phenomena.* Oxford University Press, London, 1971.

Figure captions

Figure 1: Rietveld refinement of the XRD pattern of Sn20 alloy.

Figure 2: Rietveld refinement of the XRD pattern of In20 alloy.

Figure 3: Temperature dependence of the magnetization measured at 0.05 T. The *insets* display the characteristic magnetic transition.

Figure 4: Isothermal magnetization around the Curie temperatures at different temperatures.

Figure 5: $-\Delta S_M(T)$ curves under an applied fields up to 5 T (left), and the corresponding magnetic field dependence of $-\Delta S_M^{max}$ (right).

Figure 6: Superposition of experimental $-\Delta S_M(T)$ curves and calculated ones under an applied fields up to 5 T, and the corresponding Landau's coefficient a(T), b(T) and c(T), respectively.

Figure 7: Modified Arrott plots for Sn20 alloy: isotherms of $M^{1/\beta}$ against $(H/M)^{1/\gamma}$ around T_c^A with the mean field model, 3D-Heisenberg model, 3D-Ising model and tricritical mean field model.

Figure 8: Modified Arrott plots for In20 alloy: isotherms of $M^{1/\beta}$ against $(H/M)^{1/\gamma}$ around T_c^A with the mean field model, 3D-Heisenberg model, 3D-Ising model and tricritical mean field model.

Figure 9: Relative slope (RS) as a function of temperature $(RS = S(T)/S(T_c))$ deduced from different models.

Figure 10: Temperature dependence of spontaneous magnetization $M_S(T, 0)$ and the inverse of initial susceptibility $\chi_0^{-1}(T, 0)$ around T_c^A.

Figure 11: Kouvel-Fisher plots for the spontaneous magnetization and the inverse of initial susceptibility around T_c^A.

Figure 12: Critical isotherms with the log-log plot shows in *insets*.

Figure 13: Scaling plots indicating universal curves above and below Curie temperatures for Sn20 and In20 alloys.

Figure 14: Modified Arrott plots for In20: isotherms of $M^{1/\beta}$ against $(H/M)^{1/\gamma}$ around T_c^* with the mean field model, 3D-Heisenberg model, 3D-Ising model and tricritical mean field model.

Figure 15: Temperature dependence of spontaneous magnetization $M_S(T, 0)$ and the inverse of initial susceptibility $\chi_0^{-1}(T, 0)$ around T_c^*.

Figure 16: Modified Arrott plots: isotherms of $M^{1/\beta}$ against $(H/M)^{1/\gamma}$ with $\beta = 0.43$ and $\gamma = 0.73$.

11

Figure 17: Kouvel-Fisher plots for the spontaneous magnetization and the inverse of initial susceptibility around $T_c^*(In20)$.

Figure 18: Scaling plots indicating universal curves above and below $T_c^*(In20)$.

**Figure 19:** Critical isotherm of $M(\mu_0 H, T_c^*)$ with the log-log plot shown in the *inset*.

Table caption

**Table 1:** Critical exponents values of Sn20 and In20 alloys with those of the theoretical models.

Table 1

Sample	Technique	β	γ	δ	Ref.
Sn20	MAPs	0.421±0.076	1.078±0.142	3.560±0.0661.	This work
	K-F	0.349±0.040	1.171±0.118	-	
	CI			3.710±0.007	
In20	MAP	0.461±0.032	1.170±0.206	3.537±0.174	This Work
	K-F	0.494±0.045	1.159±0.146	-	
	CI			3.439±0.007	
	MAP	0.434±0.037	0.737±0.490	2.698±0.453	
	K-F	0.466±0.050	0.702±0.043	-	
	CI			2.645±0.003	
Mean field model		0.5	1.0	3.0	[24]
3D-Heisenberg model		0.365	1.336	4.80	
3D-Ising model		0.325	1.241	4.82	
Tricritical mean field		0.25	1.0	5.0	
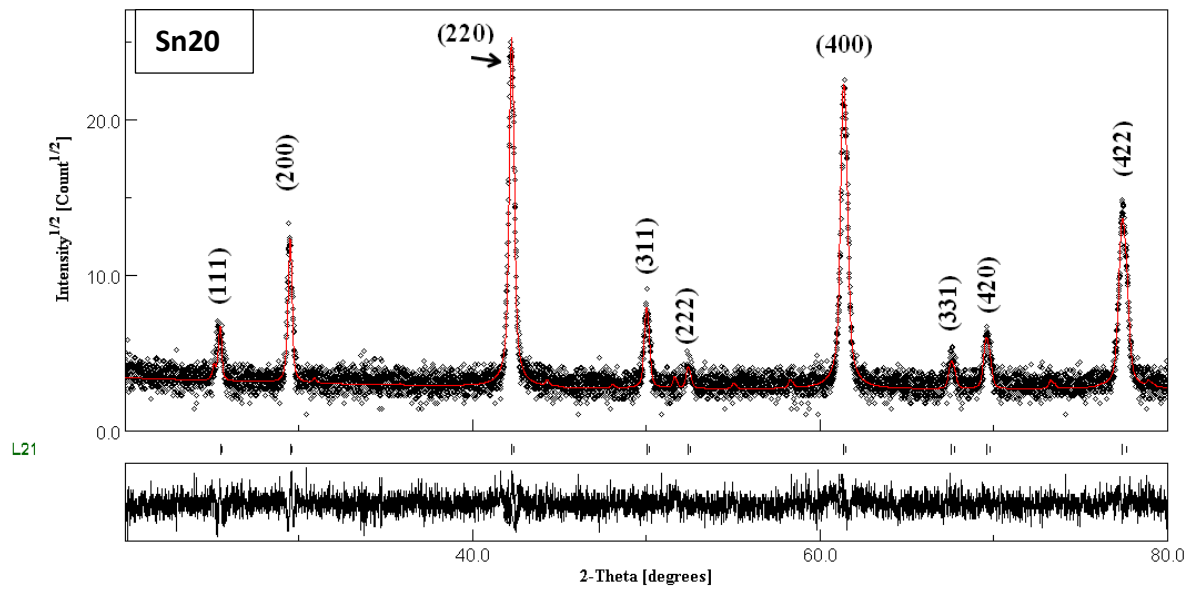
Fig.1: Rietveld refinement of the XRD pattern of Sn20 alloy.
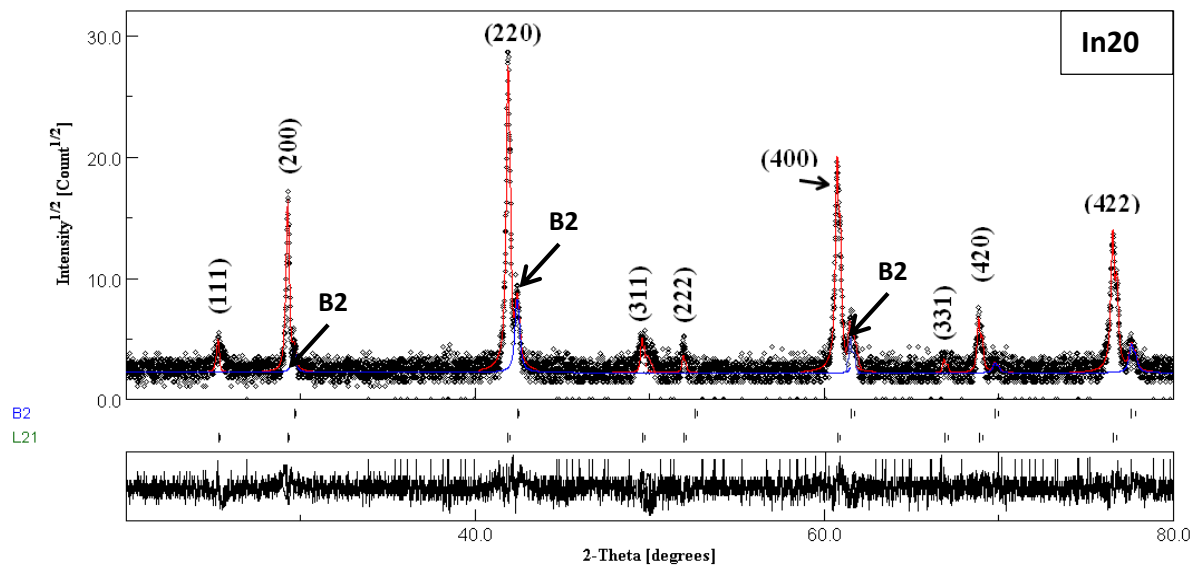
Fig.2: Rietveld refinement of the XRD pattern of In20 alloy.
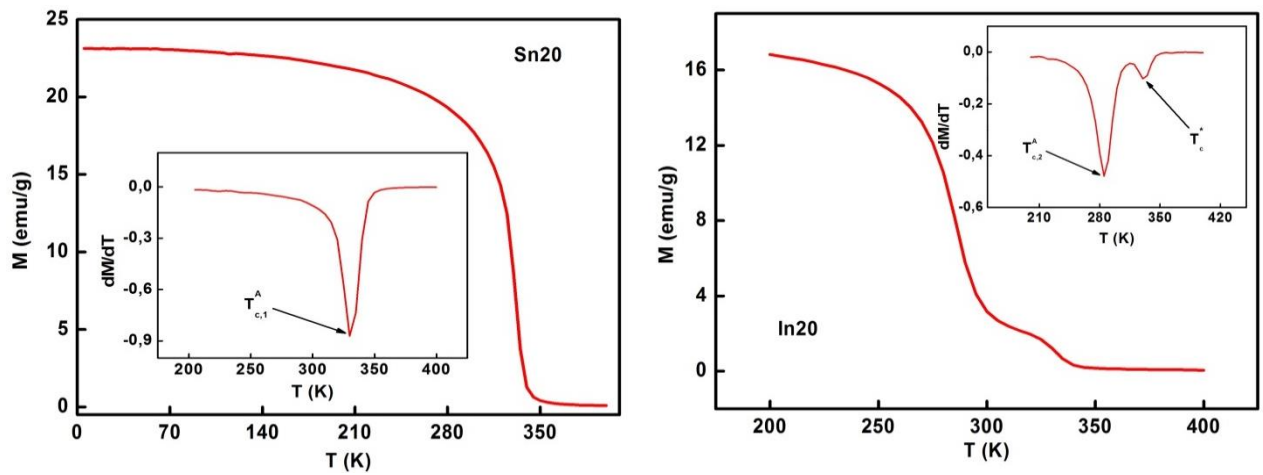
Fig. 3: Temperature dependence of the magnetization measured at 0.05 T. The characteristic magnetic transition is shown in the inset.
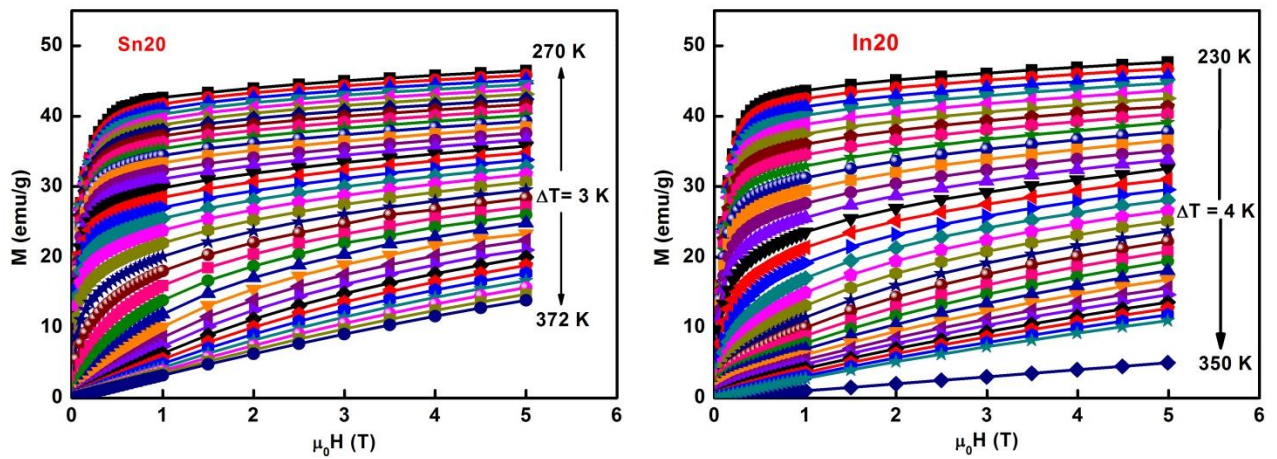
Fig. 4: Isothermal magnetization of In20 and Sn 20 alloys, around the Curie temperatures, at different temperatures.
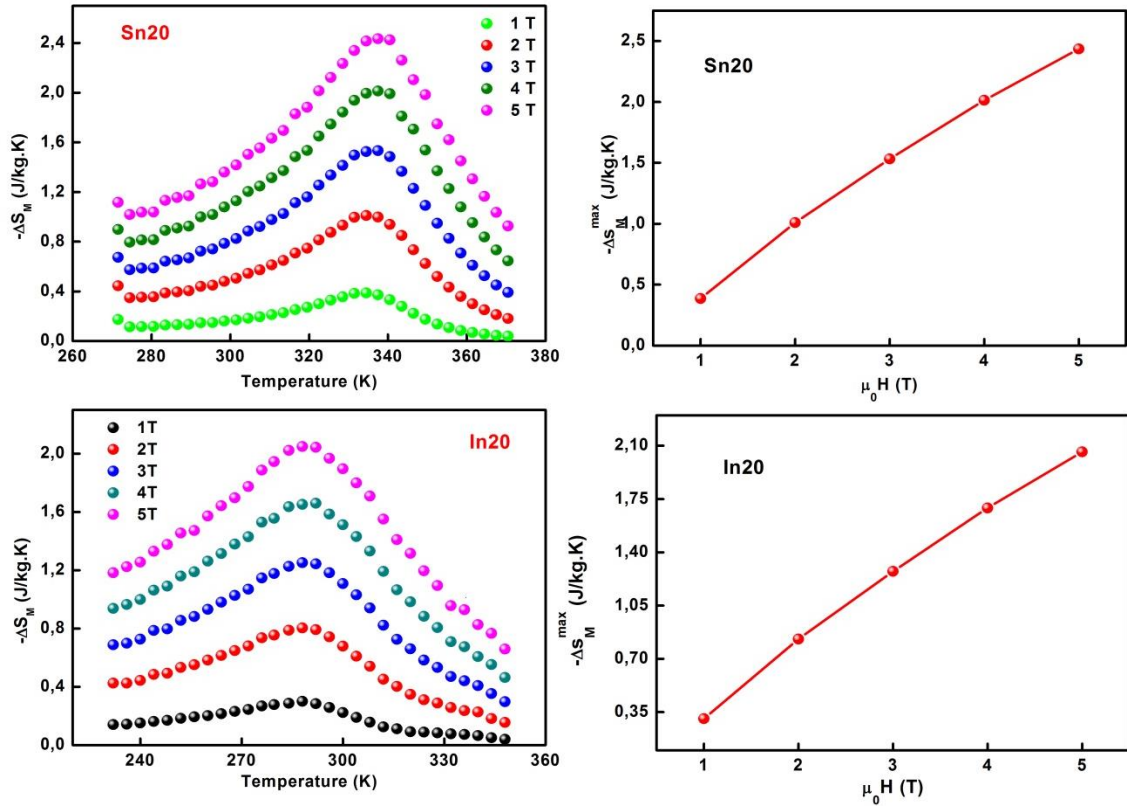
Fig. 5: $-\Delta S_M(T)$ curves under applied magnetic fields up to 5 T (left), and the corresponding magnetic field dependence of $-\Delta S_M^{max}$ (right).
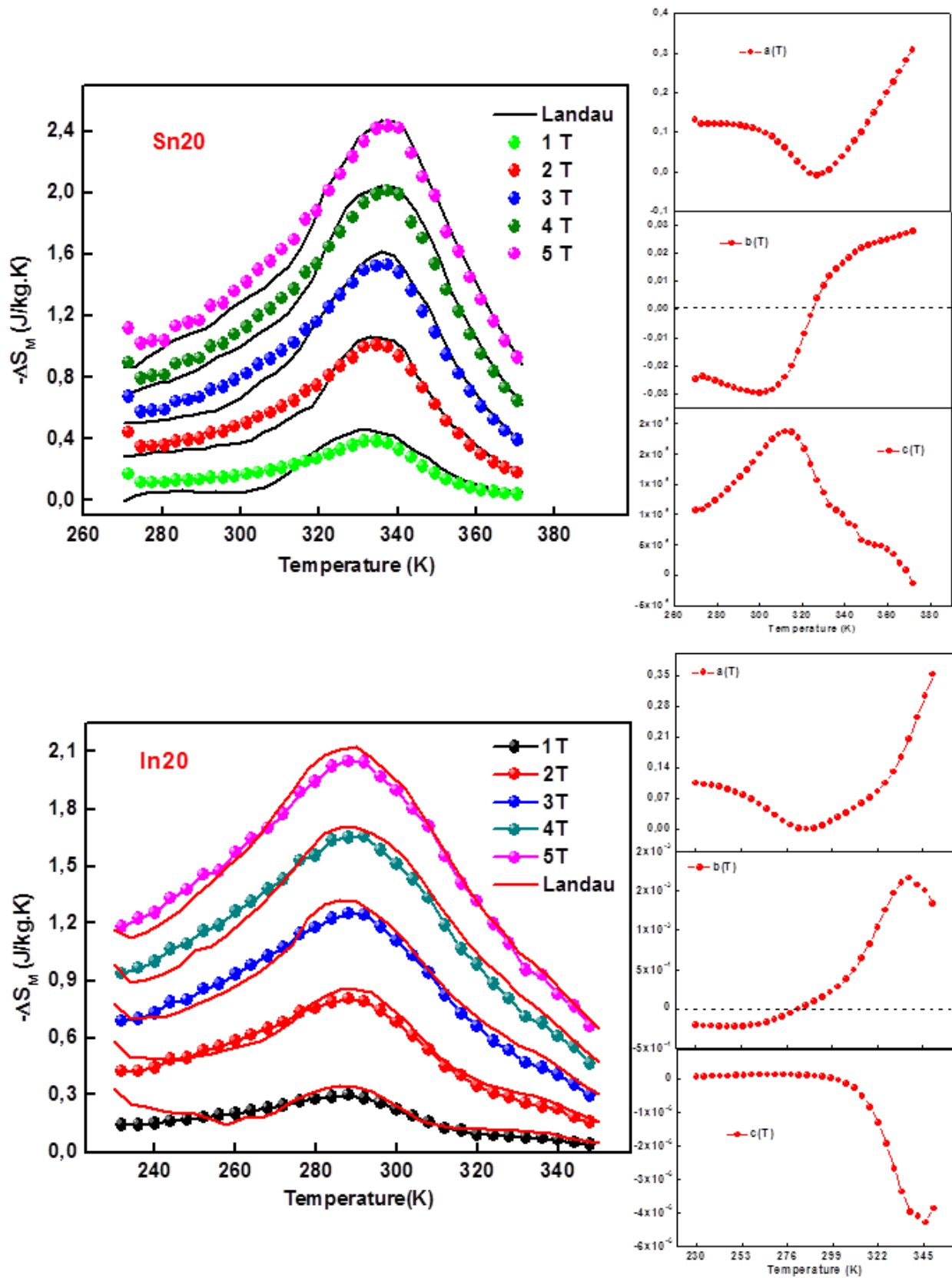
Fig. 6: Experimental and calculated $-\Delta S_M(T)$ curves under an applied field up to 5 T, and the corresponding Landau's coefficient a(T), b(T) and c(T).
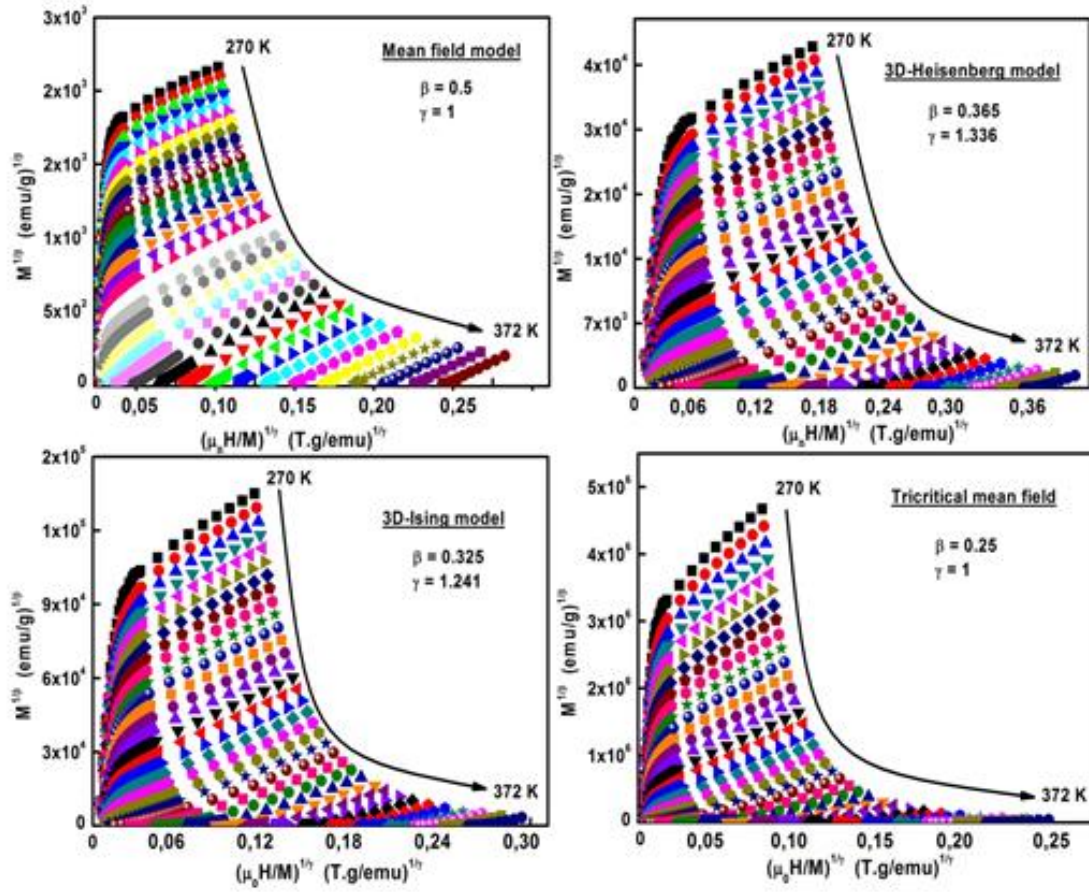
Fig. 7: Modified Arrott plots for Sn20 alloy: isotherms of $M^{1/\beta}$ against $(H/M)^{1/\gamma}$ around $T_{c,1}^{A}$ with the mean field model, 3D-Heisenberg model, 3D-Ising model and tricritical mean field model.
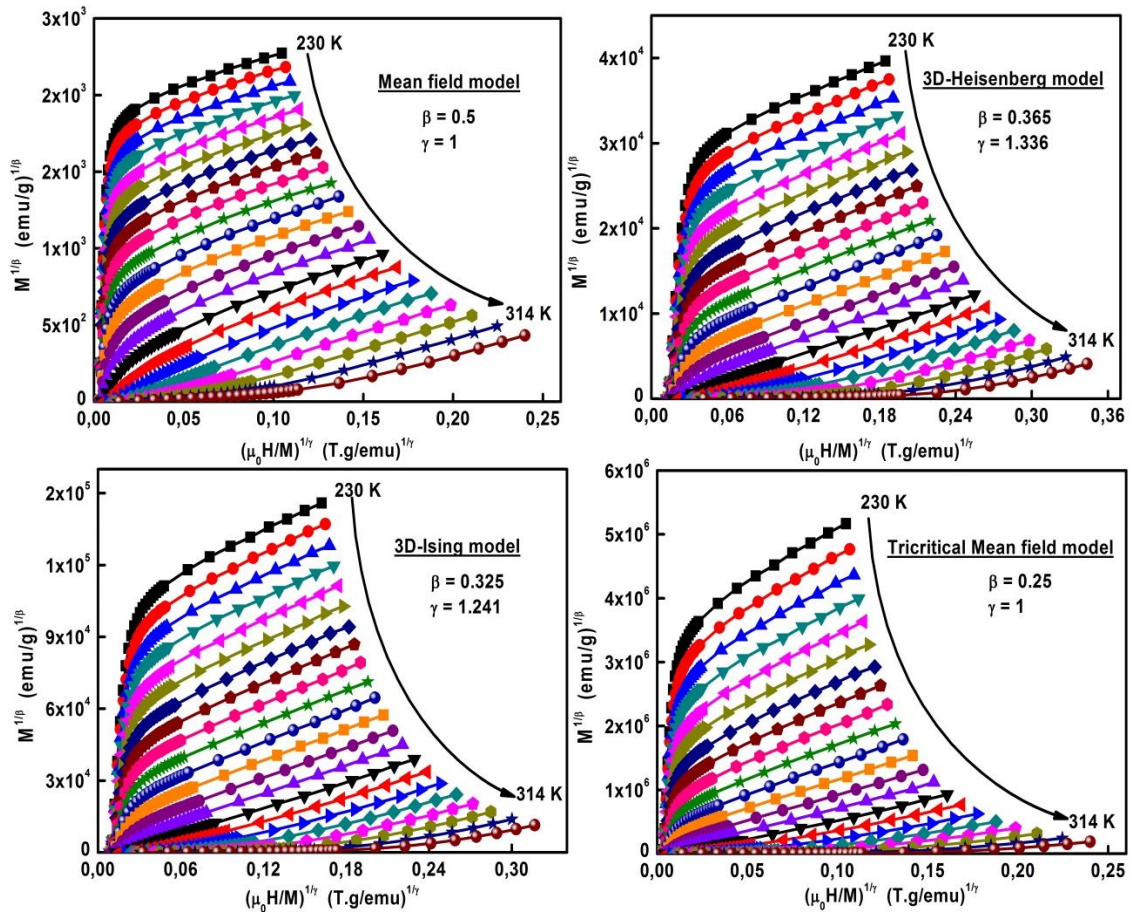
Fig. 8: Modified Arrott plots for In20 alloy: isotherms of $M^{1/\beta}$ against $(H/M)^{1/\gamma}$ around $T_{c,2}^A$ with the mean field model, 3D-Heisenberg model, 3D-Ising model and tricritical mean field model.
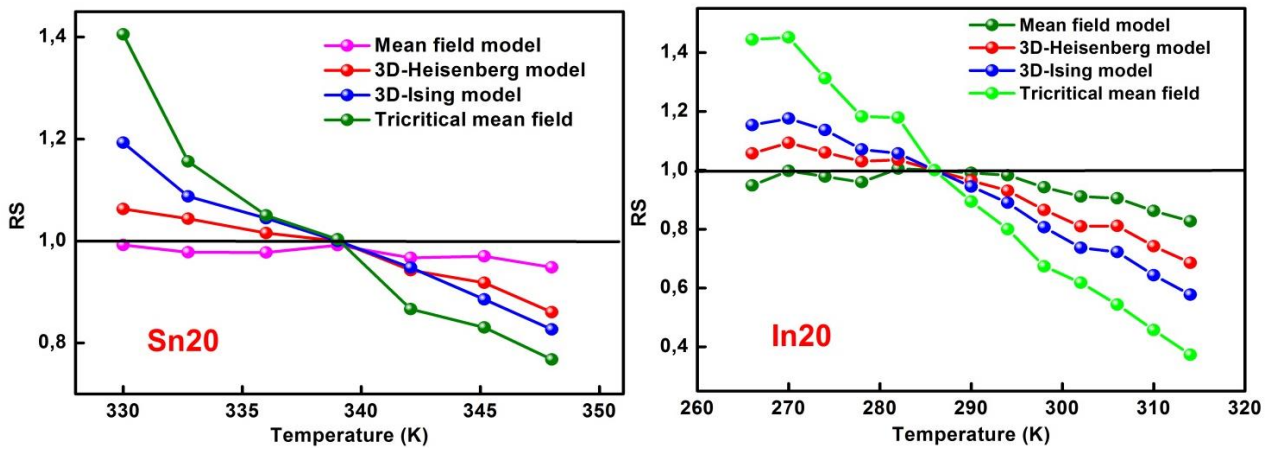
Fig. 9: Relative slope $(RS = S(T)/S(T_c))$ as a function of temperature using different models.
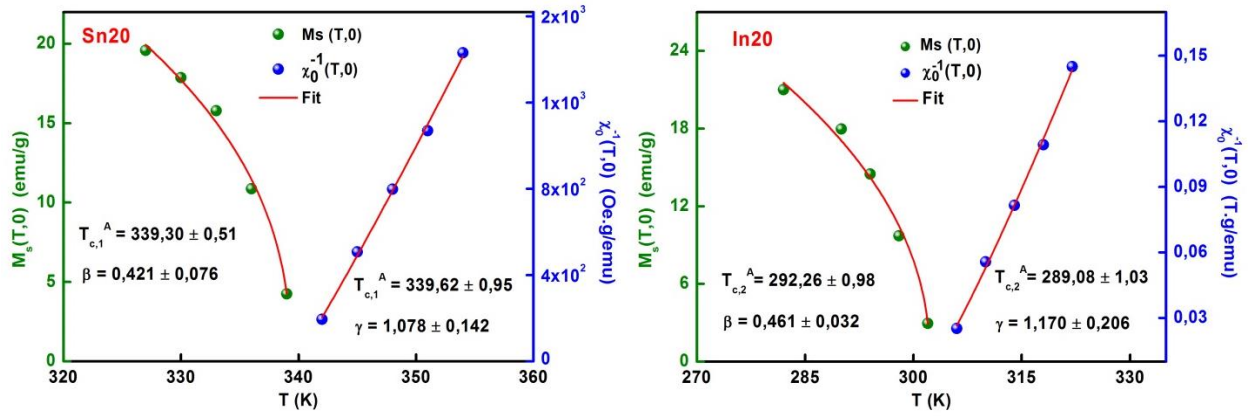
Fig. 10: Temperature dependence of spontaneous magnetization $M_S(T, 0)$ and the inverse of initial susceptibility $\chi_0^{-1}(T, 0)$ around T_c^A.
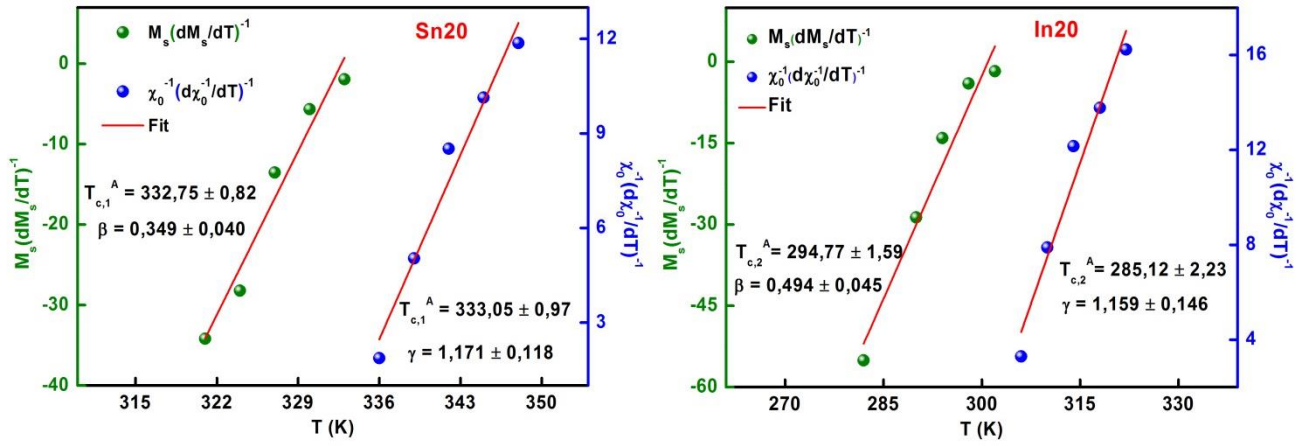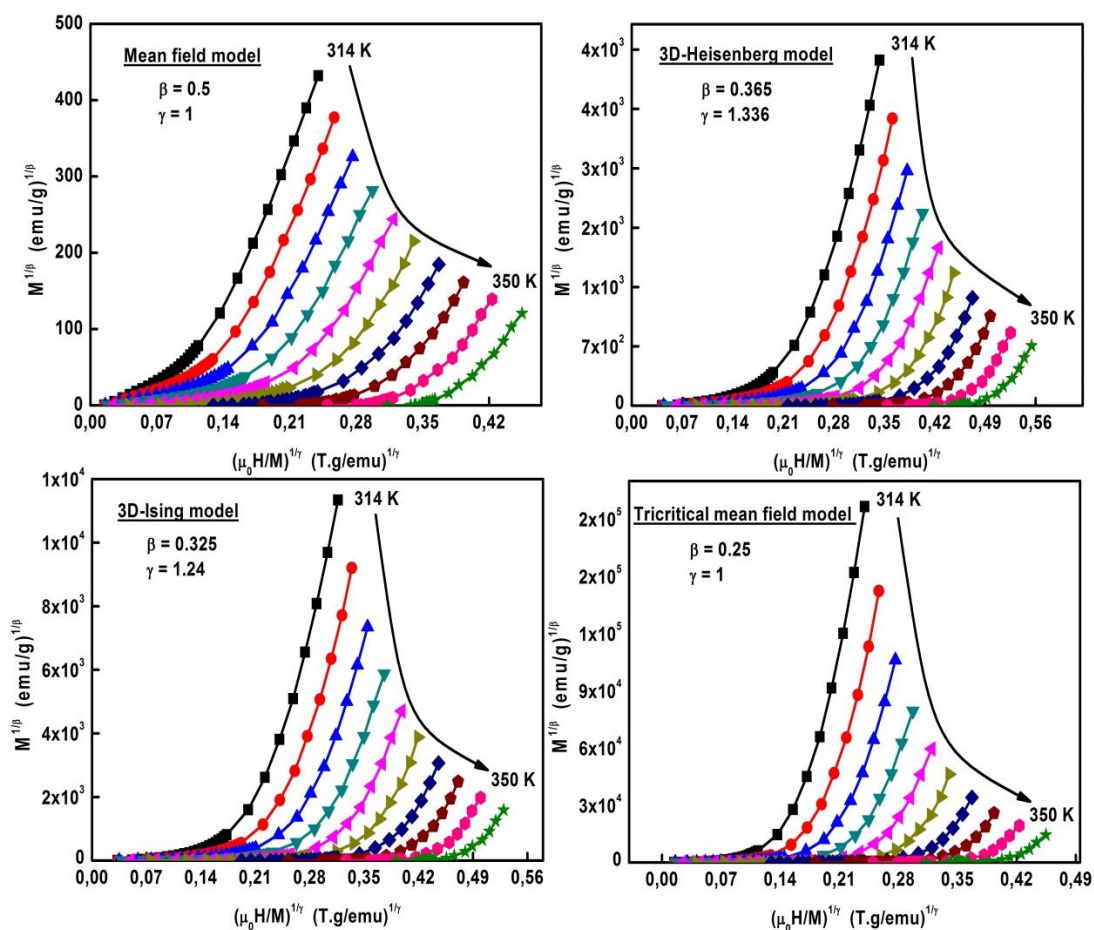

Fig. 11: Kouvel-Fisher plots for the spontaneous magnetization and the inverse of initial susceptibility around T_c^A.
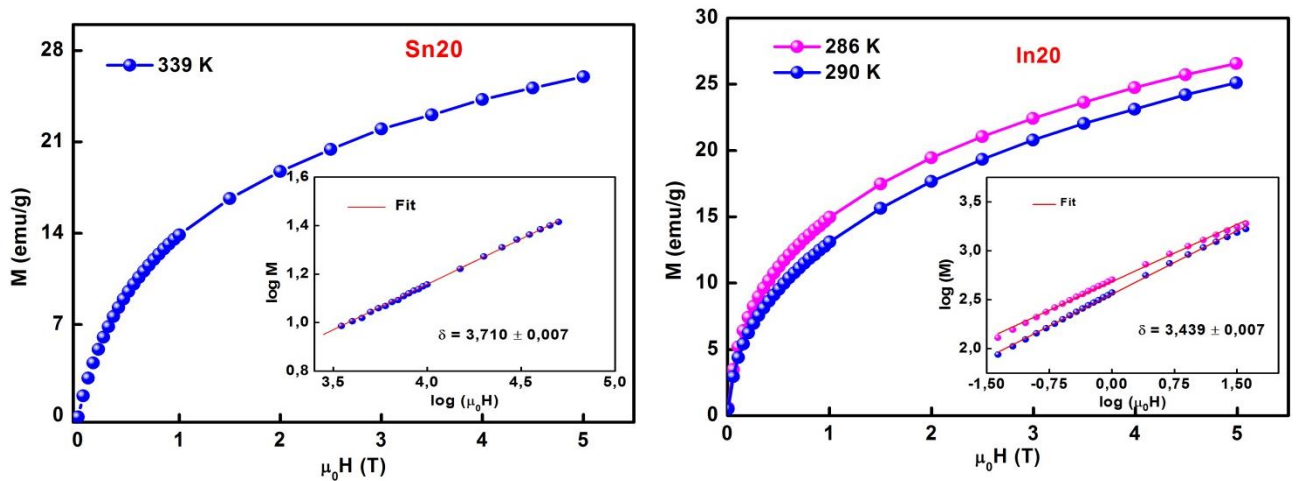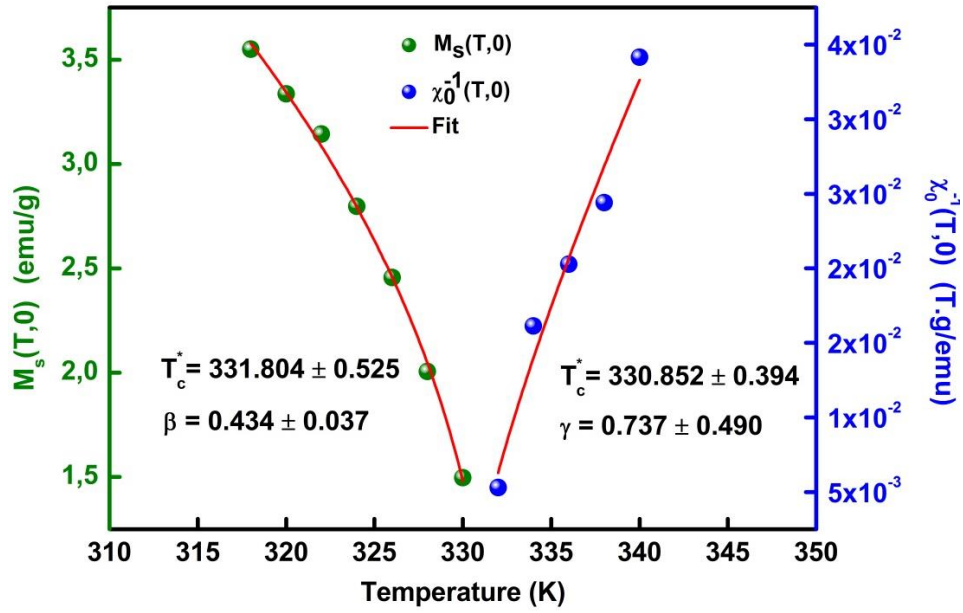

**Fig. 12:** Critical isotherms. Insets show the log-log plot.
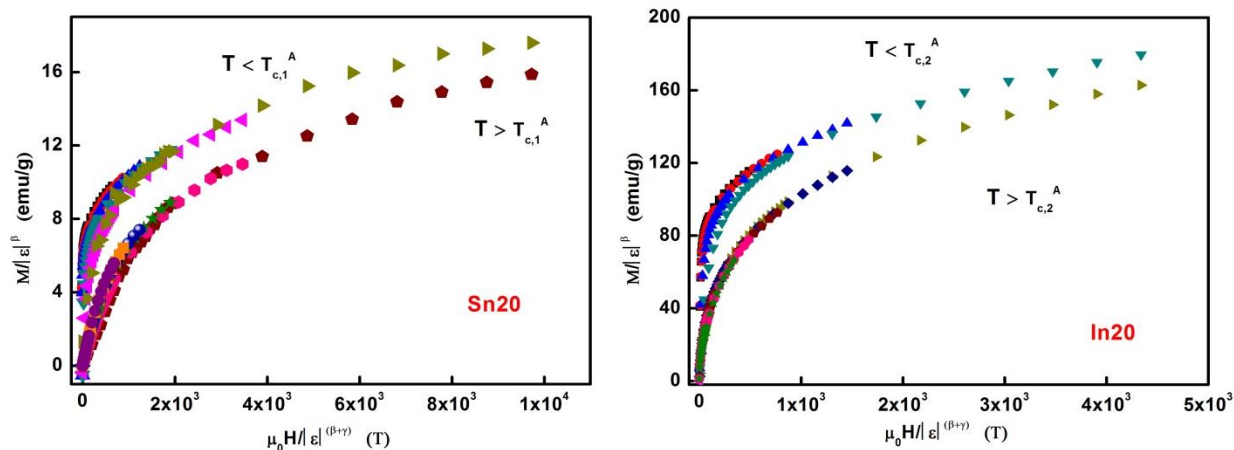
Fig. 13: Scaling plots indicating universal curves above and below
the Curie temperature for Sn20 and In20 alloys.

Fig. 14: Modified Arrott plots for In20 alloy: isotherms of $M^{1/\beta}$ against $(H/M)^{1/\gamma}$
around T_c^* with the mean field model, 3D-Heisenberg model, 3D-Ising model
and tricritical mean field model.

Fig. 15: Temperature dependence of spontaneous magnetization $M_S(T, 0)$ and the inverse of the initial susceptibility $\chi_0^{-1}(T, 0)$ around T_c^*.
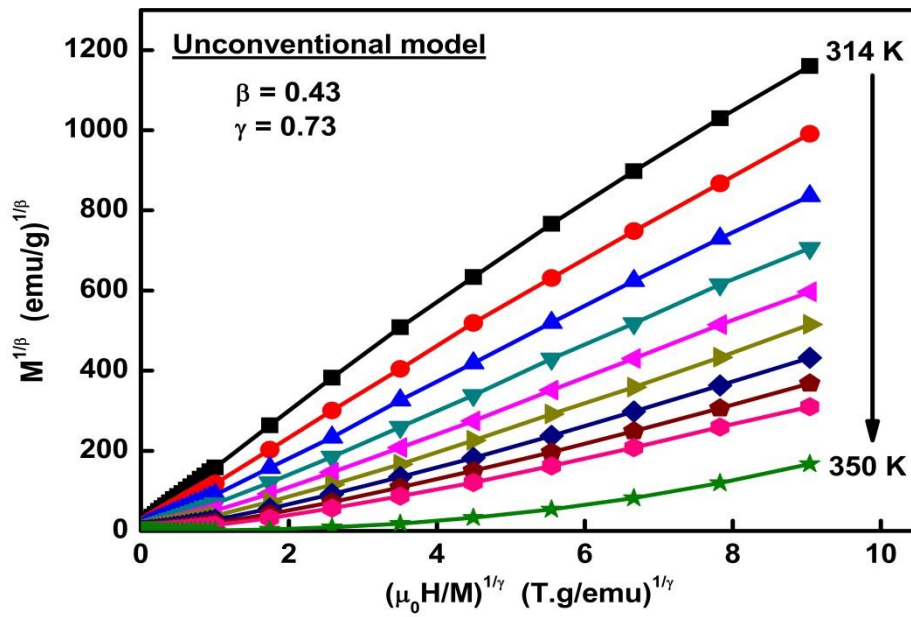
Fig. 16: Modified Arrott plots: isotherms of $M^{1/\beta}$ against $(H/M)^{1/\gamma}$ with $\beta = 0.43$ and $\gamma = 0.73$.
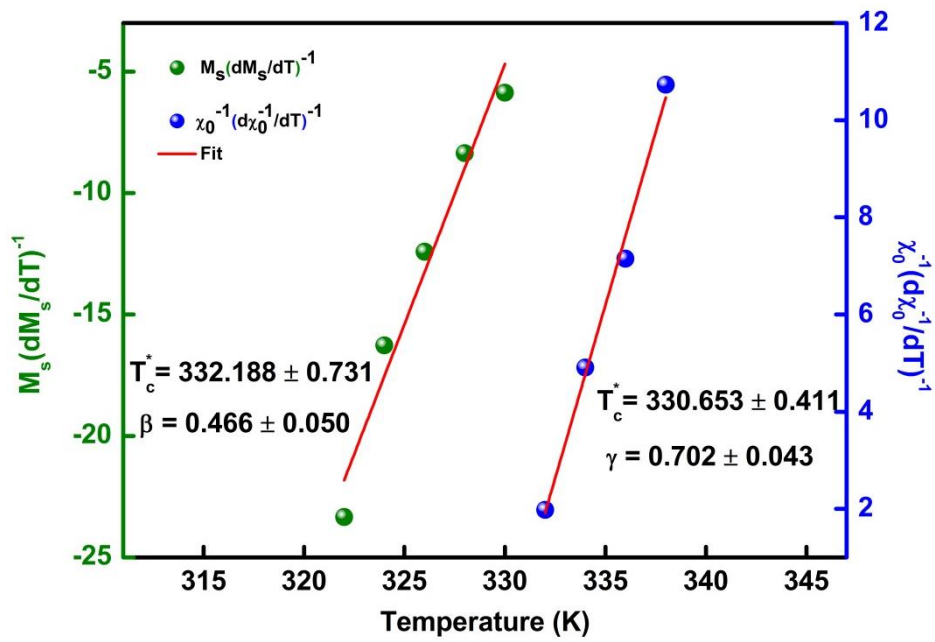
Fig. 17: Kouvel-Fisher plots for the spontaneous magnetization and the inverse of the initial susceptibility around T_c^*.
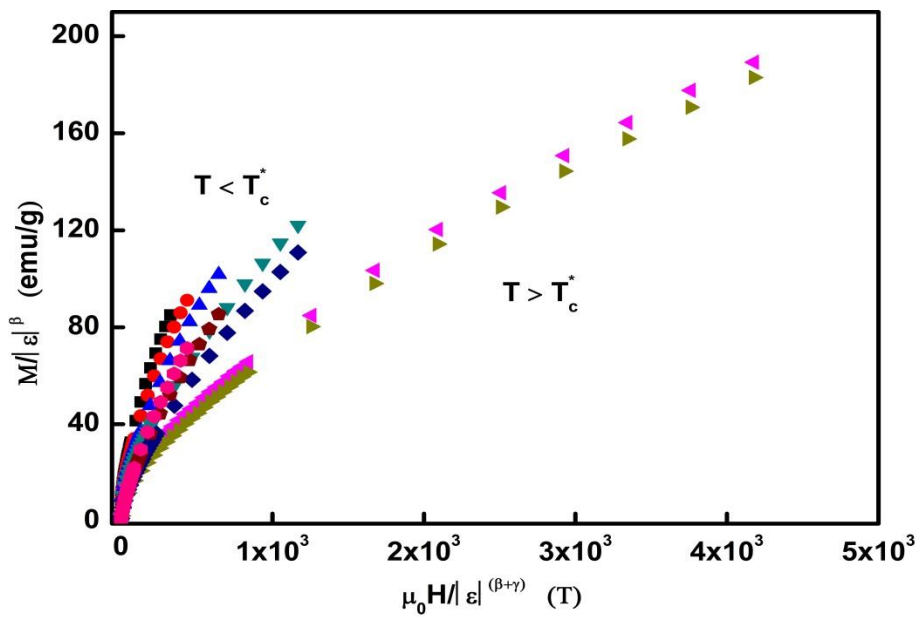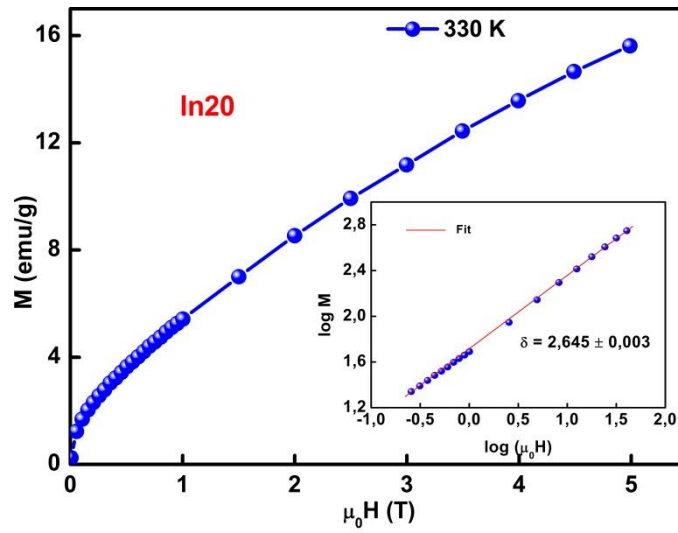

Fig. 18: Scaling plots indicating universal curves above and below T_c^*.

Fig. 19: Critical isotherm of $M(\mu_0 H, T_c^*)$. The log-log plot is shown in the *inset*.